Manufacturing of a Schwarz-P pattern by multi-axis WAAM

Sébastien Campocasso, Maxime Chalvin, Ugo Bourgon, Vincent Hugel, Matthieu Museau

Manufacturing of a Schwarz-P pattern by multi-axis WAAM

Sébastien Campocasso [a], Maxime Chalvin [a], Ugo Bourgon [a], Vincent Hugel [a], Matthieu Museau [b]

[a] *Université de Toulon, COSMER, Toulon, France*
[b] *Univ. Grenoble Alpes, CNRS, Grenoble INP, G-SCOP, 38000 Grenoble, France*

Submitted by Didier Dumur (1), CentraleSupélec, Univ. Paris-Saclay, Gif-sur-Yvette, France

With the rise of additive manufacturing, Schwarz infill patterns have been increasingly used for producing lightweight parts or improving heat exchange efficiency. Currently, metallic patterns are fabricated almost exclusively using powder bed-based processes despite the advantages of directed energy deposition (DED) technologies, namely, low cost and large dimensional capability. In this study, a framework based on iso-height layers is proposed to allow multi-axis manufacturing of a Schwarz-P pattern by wire arc additive manufacturing (WAAM). The steps involved in the computer-aided manufacturing (CAM) chain are described, followed by an experimental validation on an 8-axis robotised cell.

Additive manufacturing, Robot, Tool path

1. Introduction

Infill patterns, such as lattices or cellular materials, have been increasingly used with the development of additive manufacturing (AM) processes. Among these patterns, triply periodic minimal surface (TPMS) patterns, including Schwarz patterns, present several advantages, such as their ability to be duplicated with good continuity of the thin walls constituting the patterns. Their use in heat exchangers [1] and lightweight mechanical parts [2] has already been demonstrated.

These patterns are commonly manufactured using powder bed fusion (PBF) based AM processes [3]; directed energy deposition (DED) processes have not been used despite their advantages so far. Among the DED processes, robot-based wire arc additive manufacturing (WAAM) offers high productivity and large manufacturing volumes at low investment and consumable costs [4].

WAAM applications are generally limited to fabrication of rib-type structures [5] or simple thin-wall geometries such as revolving shapes. Cellular materials are typically considered to be outside the scope of WAAM applications [5] or limited to extruded metamaterials [6], such as honeycombs. However, recent studies have explored drop-by-drop WAAM of lattices [7]. A proposal for 3D pattern–based metamaterials [6] should also be noted, but in this case, the pattern is filled with a second material that serves as support. No DED manufacturing of TPMS patterns has been attempted thus far, whereas the topology of sheet-based TPMS patterns made up of thin walls [1] seems to be well adapted for DED manufacturing in continuous welding bead deposition. However, the success of such complex fabrication requires a multi-axis approach to avoid the need for support materials [8, 9]. Therefore, the objective of the present study is to evaluate the manufacturability of a Schwarz primitive (Schwarz-P) pattern by multi-axis WAAM. This pattern is shown in Fig. 1 and approximately mathematically defined by an implicit equation [10] given by Eq. (1), where L_p is the length of the pattern bounding box.

$$\cos\left(x \cdot \frac{2\pi}{L_p}\right) + \cos\left(y \cdot \frac{2\pi}{L_p}\right) + \cos\left(z \cdot \frac{2\pi}{L_p}\right) = 0 \qquad (1)$$

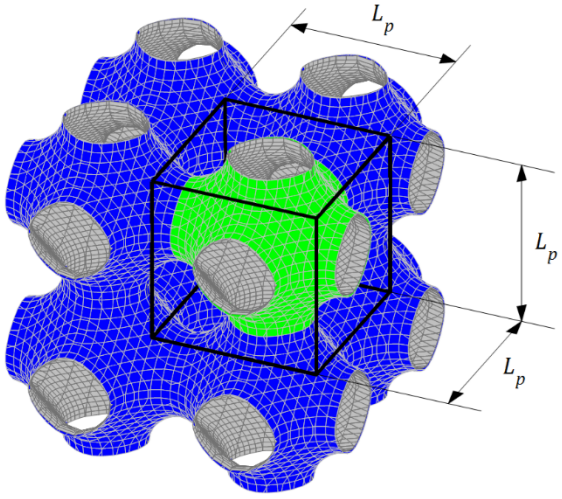

Figure 1. Schwarz-P pattern (green colored) within a pattern assembly.

To manufacture this pattern with a robot-based WAAM device, several steps, starting with the generation of an iso-height layer deposition path and ending with optimised multi-axis robotic motions, were developed and grouped within a framework presented in Section 2. The experimental work is described in Section 3, followed by a discussion. Section 4 concludes this study.

2. Multi-axis DED framework

The originality of the approach based on the framework shown in Fig. 2 lies in the use of continuous multi-axis deposition with iso-height layers, which allows the use of constant welding parameters.

In the first stage (Steps 1 and 2), an initial trajectory composed of the deposition path (points *P*) and local orientation (vectors ***b***) is calculated. This first stage would basically correspond to the CAM software. However, because of the resulting complex relative motions, this initial trajectory cannot be used as is.

The second stage, called 'Pre-processing', is composed of Steps 3 to 5, whose objectives are to smooth the robot/positioner motions

and avoid collisions (at least between the deposition tool and in-process workpiece), which are two classical goals in multi-axis deposition [9, 11]. Because these steps are now performed in the basis linked to the part, this stage can be integrated into the CAM software. However, it is also possible to perform them after Step 6 to directly smooth the joint motions and thus consider possible collisions between the robotic arm parts and workpiece.

The third stage is dedicated to the robotic structure used and is classically called 'Post-processing'. Step 6 involves the application of an inverse geometric model (IGM) to calculate the joint coordinates. Step 7 optimises the joint motion using the redundancies of the structure (if any). Finally, Step 8 addresses the problems linked to singularities before generating a manufacturing program for the robot (Step 9). The main steps of the methodology are described in the following subsections.

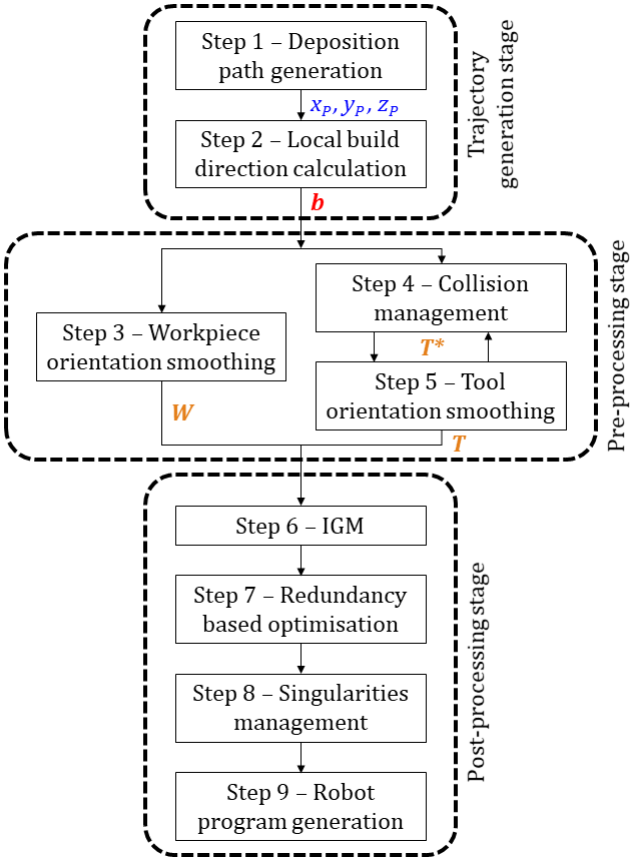

Figure 2. Proposed multi-axis DED framework.

2.1. Trajectory generation stage: iso-height layer deposition path generation and local build direction calculation

The deposition path is defined as the 3D curve followed by the deposition tool tip. The path is calculated to have a constant local inter-layer distance h_{Layer} (layer height). This strategy allows manufacturing complex shapes with constant deposition parameters, as explained in [12, 13].

In the present study, the path is obtained from an analytical parameterisation of the eighth pattern surface divided vertically (eighth corresponding to the green part in Fig. 3); however, it can also be obtained from a meshed file of the full pattern [14]. The parameterisation used is given by Eq. (2) for the Z_{Part} direction but can be applied for each of the three directions, that is, X_{Part}, Y_{Part}, and Z_{Part}, owing to the symmetries of the pattern.

Using this parameterisation, the path is calculated point-by-point using an optimisation algorithm under constraints, which determines the values of parameters u and v such that the distance between the point and previous layer is the closest possible to h_{Layer} and located at approximately L_{Seg} from the previous point of the current layer (segment length, in Fig. 6). Initialisation is performed with the first point of each layer calculated for $u = 0$, and the last point is calculated for $u = 1$.

Once the path for the eighth pattern is obtained, it is first duplicated by symmetry. Then, the first quarter is duplicated three times by rotation, as displayed in Fig. 3.

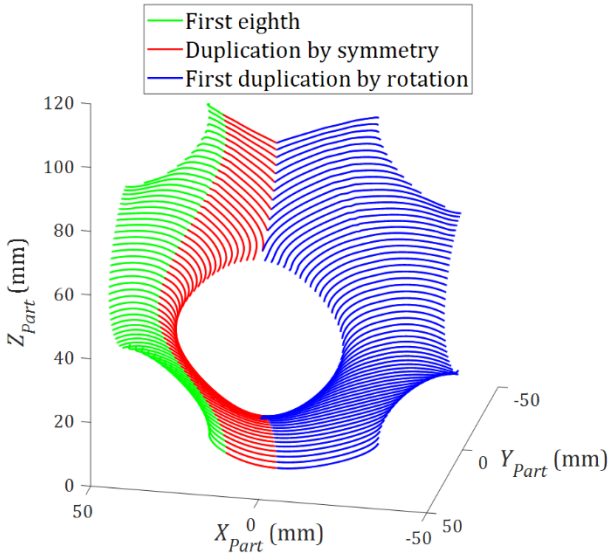

Figure 3. Generation of the deposition path with a constant local inter-layer distance (only half of the pattern for better readability); see also [14].

At each point P (coordinates x_P, y_P, and z_P) of the deposition path, a local vector $\boldsymbol{b}$ corresponding to the local direction of the layer stacking is defined and called the build direction. This vector $\boldsymbol{b}$ was previously defined as the cross product between vector $\boldsymbol{t}$ (tangent to the deposition path) and vector $\boldsymbol{n}$ (normal to the part surface) [8]; a similar approach was used in [12]. The build directions for half of the Schwarz-P pattern are shown every three layers in Fig. 4 for better readability.

The basic idea is to use the robotic system to keep vector $\boldsymbol{b}$ vertical such that the melting pool remains horizontal with the previously built wall below [15, 16]. Usually, the tool axis $\boldsymbol{T}$ is set coaxial with $\boldsymbol{b}$ or may be inclined with constant lead and tilt angles.

Finally, the full $(\boldsymbol{t}, \boldsymbol{n}, \boldsymbol{b})$ basis is used for the collision management step presented in Section 2.2.

$$\begin{cases} x(u,v) = \dfrac{L_p}{2\,\pi}\left\{\operatorname{acos}\left[-\operatorname{sign}(\cos v)\,.\,\left(\dfrac{|\cos v|}{2}\right)^{1-\frac{u}{2}}\right] + \operatorname{acos}\left[\left(\dfrac{|\cos v|}{2}\right)^{\frac{u}{2}}\right]\right\} \\ y(u,v) = \dfrac{L_p}{2\,\pi}\left\{\operatorname{acos}\left[-\operatorname{sign}(\cos v)\,.\,\left(\dfrac{|\cos v|}{2}\right)^{1-\frac{u}{2}}\right] - \operatorname{acos}\left[\left(\dfrac{|\cos v|}{2}\right)^{\frac{u}{2}}\right]\right\} \\ z(u,v) = \dfrac{L_p}{2\,\pi}\,.\,v + \dfrac{L_p}{2} \end{cases} \quad with \quad \begin{cases} u \in [0;1] \\ v \in [-\pi;\pi] \end{cases} \tag{2}$$

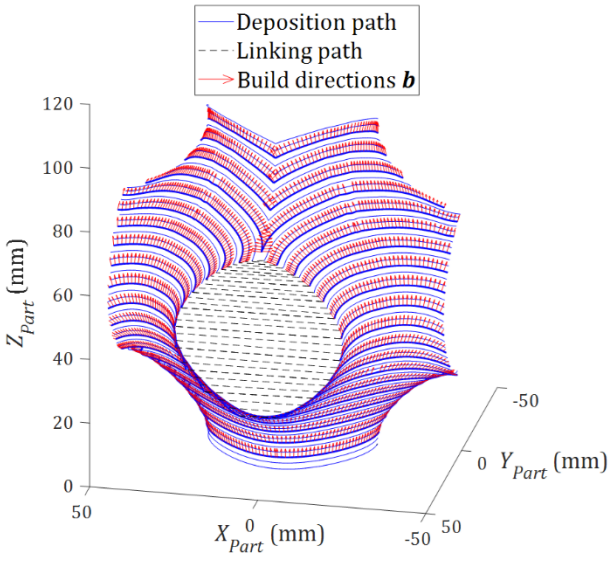

Figure 4. Initial local build direction vectors (shown every three layers for half of the pattern).

2.2. Pre-processing stage: orientation smoothing and tool/workpiece collision management

From the ***b*** vectors, a first orientation smoothing is conducted to reduce jerky motions related to the workpiece orientation and thus improve quality [17]. When the angle between two consecutive orientations is greater than 10°, linear smoothing is locally applied to the ***b*** vectors over a length of 10 mm before and after discontinuity (Fig. 5 (a)). The new vectors, denoted ***W*** (Fig. 5 (b)), can then be used to calculate the two joint coordinates of the 2-axis positioner so that these vectors ***W*** are vertical. Thus, the ***W*** vectors represent the workpiece orientation.

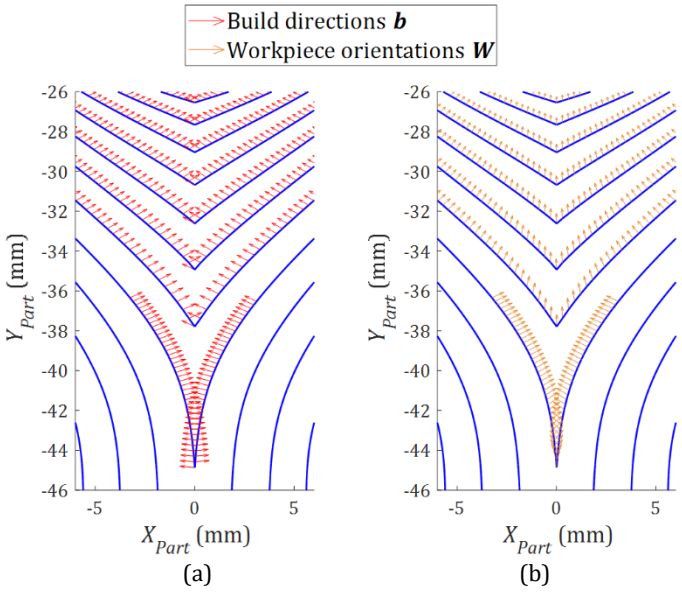

Figure 5. Workpiece orientations: (a) before smoothing (similar to the build directions shown in Fig. 4) and (b) after smoothing.

To detect and avoid collisions between the welding tool and workpiece, a bead geometrical model based on half-ellipses drawn in local (***n***, ***b***) planes is used. At each point of the path, the major axis of the ellipse is equal to the bead width w_{Bead} and is oriented by ***n***, whereas the semi-minor axis is equal to h_{Layer} along ***b***.

As depicted in Fig. 6, the welding torch is modelled by a cylinder and the collision avoidance consists of calculating locally the optimal tilt angle θ_t about ***t*** so that the previously deposited beads are outside this cylinder. This step is followed by smoothing (similar to that presented previously) to determine the tool orientations ***T*** from the ***b*** vectors via a transient vector **T***, with some iterations if the smoothing leads to new collisions.

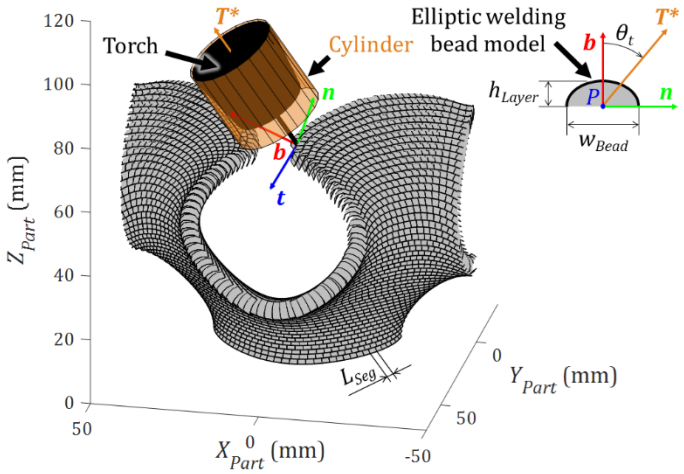

Figure 6. Welding bead section modelling and collision avoidance by tilting about ***t*** vector to obtain **T*** vector (i.e. tool orientation before Step 5).

2.3. Post-processing stage

The IGM of Step 6 was determined analytically. It allows calculating the two positioner coordinates such that ***W*** is vertical at each time and the six robot coordinates such that ***T*** is well oriented and the tool tip well-positioned relative to the workpiece.

Step 7 involves optimising the robot motions when using a coaxial deposition tool allowing to change the self-rotation about vector ***T*** [13], which relies on one degree of freedom or redundancy.

Finally, the singularity of the positioner (when the table is tilted from one side to the other through the horizontal position) is managed in Step 8 using a patch curve, as proposed in [18], to avoid incoherent motions of the last joint.

3. Experimental validation

3.1. Experimental set-up

The manufacturing experiments were conducted using a robotic cell from Fanuc (Fig. 7), which is controlled by an R30iB+ controller and composed of a 6-axis 120iC welding robot and 2-axis positioner used in a continuous motion manner. The welding source was TPS500i CMT (Fronius).

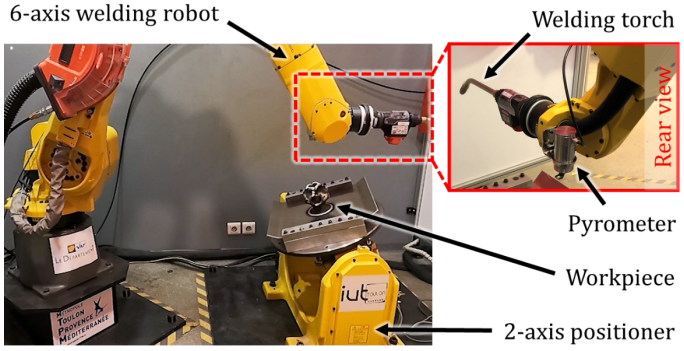

Figure 7. Experimental device during temperature measurement cycle.

Aluminium alloy AA 5183 (wire Φ1.2 mm) was deposited on an AA 5086 substrate (4 mm thick) with argon shielding gas (99.9% pure, 18 L/min flow). The travel speed (TS) and wire feed speed (WFS) were constant and set to 55 cm/min and 5 m/min, respectively; WFS = 6.5 m/min for the first layer on the substrate.

Between two consecutive layers, cooling breaks were implemented. The cooling time varied depending on the temperature measured by the Optris CTlaser 3MH1 CF3 pyrometer shown in Fig. 7. The threshold temperature was set to 160°C.

3.2. Experiment

The experiment involved manufacturing a single Schwarz-P pattern of 100 mm length (L_p) with a single bead wall thickness (approximately corresponding to w_{Bead} = 5.5 mm with the deposition parameters used). The layer height h_{Layer} was set to 1.95 mm for the path generation and $L_{Seg} \approx 1$ mm.

To avoid collisions between the torch and clamping system, the first-layer path was repeated ten times, as shown in Fig. 8. A preheating welding bead was placed around the first layer to obtain an initial suitable substrate temperature.

For the first and fourth quarters (bottom and top) of the pattern, the layers correspond to closed-loop curves. In this case, the deposition was performed in the same direction for all layers, and the start/stop points were shifted from a polar angle of 37° from one layer to the next. In the second and third quarters (altitudes corresponding to the four horizontal holes), one layer corresponds to the four separate walls. In this case, the deposition was performed by reversing the direction from one layer to the next to compensate for the start and stop defects as much as possible.

3.3. Results and discussion

As shown in Fig. 8, the proposed method allowed the fabrication of a first Schwarz-P pattern using WAAM. The quality is relatively good for the first three quarters from the bottom. As highlighted in Fig. 8, the main problems appear at the junction between the four walls built separately in the second and third quarters (divided horizontally). There, two problems are encountered.

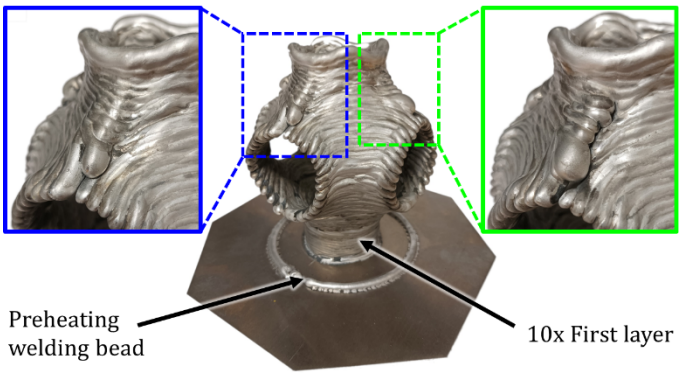

Figure 8. Part (L_p = 100 mm) manufactured in 2 h 27 min (76 % for cooling).

The first one comes from the deposition path with two difficulties:

- A huge tangency discontinuity remains a source of defects, even after orientation smoothing, owing to the speed change and lateral bead self-overlap [19], leading to an over-deposit.
- The distance between the two beads is not well mastered because both are calculated separately from the previous layer without considering the other one; therefore, the result varies depending on the values of L_p and h_{Layer}.

The second problem is related to the deposition of a new bead, which must weld two walls built separately using WAAM. Owing to geometrical defects, most of the time, only one side attracts the electric arc and the new bead overlaps only one of the walls. Suitable strategies must be employed for the wall junctions [20].

4. Conclusion

In this study, a CAM chain for multi-axis DED AM was proposed to obtain optimised robot motions from a complex surface to be manufactured. The framework was successfully used to manufacture thin-walled Schwarz-P patterns using WAAM, which opens up new possibilities for the fabrication of large heat exchangers or lightweight components.

Future efforts will focus on obtaining a pattern assembly, which is still a challenge considering thermal management, further collisions, and joint motion dynamics that will be even more complex with patterns not centred on the positioner last axis. In this study, the serial structure of the positioner was not efficient enough to allow rapid orientation changes. One possible solution is to replace this device with a parallel kinematic or redundant structure with higher dynamics. Another perspective is the fabrication of variable-density pattern assemblies [2], e.g. by varying the wall thickness with a weaving strategy.

Acknowledgements

This work is supported by the ANR BeShape project of the French Agence Nationale de la Recherche, Paris, France (grant number ANR-18-CE10-0014). The authors would also like to thank Lewis Andurand for his contribution relative to the path generation.

References

[1] du Plessis A, et al., 2021, Properties and applications of additively manufactured metallic cellular materials: A review, Progress in Materials Science, 125/100918:1-43.
[2] Ramírez EA, Béraud N, Pourroy F, Villeneuve F, Museau M, 2021, Design parameters effects on relative density of triply periodic minimal surfaces for additive manufacturing, Procedia CIRP, 100:13-18.
[3] Zhang Y, Tan S, Ding L, Bernard A, 2021, A toolpath-based layer construction method for designing & printing porous structure, CIRP Annals, 70/1:123-126.
[4] Williams SW, Martina F, Addison AC, Ding J, Pardal G, Colegrove P, 2016, Wire+ arc additive manufacturing, Materials Science and Technology, 32/7:641-647.
[5] Lockett H, Ding J, Williams S, Martina F, 2017, Design for Wire + Arc Additive Manufacture: design rules and build orientation selection, J Eng Design, 28:568-598.
[6] Ding Y, Akbari M, Gao XL, Ai L, Kovacevic R, 2018, Use of a robotized laser powder-feed metal additive manufacturing system for fabricating metallic metamaterials. In Manufacturing Techniques for Materials, CRC Press, 51-65.
[7] Li Y, Yu S, Chen Y, Yu R, Shi Y, 2020, Wire and arc additive manufacturing of aluminum alloy lattice structure, Journal of Manufacturing Processes, 50:510-519.
[8] Chalvin M, Campocasso S, Baizeau T, Hugel V, 2019, Automatic multi-axis path planning for thinwall tubing through robotized wire deposition, Proc CIRP, 79:89-94.
[9] Bhatt PM, et al., 2020, Building free-form thin shell parts using supportless extrusion-based additive manufacturing, Additive Manufacturing, 32/101003:1-15.
[10] Von Schnering HG, Nesper R, 1991, Nodal surfaces of Fourier series: fundamental invariants of structured matter. Zeitschrift für Physik B, 83:407-412.
[11] Plakhotnik D, et al., 2019, CAM planning for multi-axis laser additive manufacturing considering collisions, CIRP Annals, 68/1:447-450.
[12] Flores J, Garmendia I, Pujana J, 2019, Toolpath generation for the manufacture of metallic components by means of the laser metal deposition technique. The International Journal of Advanced Manufacturing Technology, 101/5:2111-2120.
[13] Chalvin M, Campocasso S, Hugel V, Baizeau T, 2020, Layer-by-layer generation of optimized joint trajectory for multi-axis robotized additive manufacturing of parts of revolution, Rob Comput Integr Manuf, 65:101960.
[14] Andurand L, Hugel V, Campocasso S, Museau M, In Press, Support-free-material path generation for DED processes from facetized data, Procedia CIRP (ICME'22).
[15] Campocasso S, et al., 2018, A framework for future CAM software dedicated to additive manufacturing by multi-axis deposition, Procedia CIRP, 78:79-84.
[16] Gibson BT, et al., 2022, Controls and process planning strategies for 5-axis laser directed energy deposition of Ti-6Al-4V using an 8-axis industrial robot and rotary motion, Additive Manufacturing, 58/103048:1-18.
[17] Chalvin M, Wulle F, Campocasso S, Elser A, Hugel V, Verl A, 2022, Orientation smoothing in multi-axis additive manufacturing, Procedia CIRP, 107:357-362.
[18] Grandguillaume L, Lavernhe S, Tournier C, 2016, A tool path patching strategy around singular point in 5-axis ball-end milling, Int J Prod Res, 54/24:7480-7490.
[19] Ding D, et al., 2021, A shape control strategy for wire arc additive manufacturing of thin-walled aluminium structures with sharp corners, J Manuf Process, 64:253-264.
[20] Yuan L, Pan Z, Polden J, Ding D, van Duin S, Li H, 2022, Integration of a multi-directional wire arc additive manufacturing system with an automated process planning algorithm, Journal of Industrial Information Integration, 26/100265:1-11.